INTERFACIAL AREA DENSITY MEASUREMENT USING A THREE-LAYER WIRE-MESH SENSOR

H.-M. Prasser, S. Stucki, T. Betschart and J. Eisenberg
Eidgenössische Technische Hochchule Zürich, ETHZ
ML K13, Sonneggstrasse 3, CH-8092 Zurich, Switzerland
hprasser@ethz.ch; B@institute.gov; torsten.betschart@psi.ch

ABSTRACT

The interfacial area density in a gas-liquid two-phase flow is measured by a wire-mesh sensor. The Euclidian norm of the gradient of the measured volumetric gas fraction is interpreted as local instantaneous interfacial area density. Averaged over a sequence of measurements, the interfacial area density of the two-phase flow is found. A three-layer sensor is used, which consists of a transmitter grid in the center and two orthogonal receiver grids above and below the transmitter grid. Such a sensor has two sensitive layers: (1) between the first receiver grid in flow direction and the transmitter grid and (2) between the transmitter and the second receiver grid. Two lateral components of the local instantaneous gas fraction gradient are approximated by the difference of the measured gas fractions between a pair of adjacent points in the measuring matrix of the first sensor, while the third component is obtained from the difference between the both sensitive layers. For experimental validation, a sensor was exposed to solitary air bubbles rising in a water tank at ambient conditions. The results are compared to information from high-speed camera images of the bubbles. Besides the interfacial area, also the bubble size extracted from both camera and sensor data was compared. Furthermore, alternatives are discussed, which may be used to estimate the interfacial area density in cases where only a wire-mesh sensor with a single measuring plane is available.

KEYWORDS
Gas-liquid flow, Interfacial area density, wire-mesh sensor, instrumentation

1 INTRODUCTION

The interfacial area density is a parameter needed to calculate energy and mass fluxes at the interface between two phases. It is needed to close momentum and energy conservation equations in a two-fluid model of a gas-liquid flow. The concept of adding interfacial area transport equations to the set of conservation equations for mass, momentum and energy is a way to consider the dynamics of the gas-liquid interface. The local instantaneous formulation of the interfacial area concentration was introduced by Kataoka et al. [1]. There are efforts to implement it in 1D thermal hydraulic codes widely used for nuclear safety analyses and it seems a promising approach for 3D two-phase CFD modelling as well. The interfacial area density can be divided into bubble-size classes, which allows a better reflection of the flow structure at higher gas fractions [2-4]. The transport equations for integral interfacial area concentrations contain source and sink terms. In an adiabatic bubbly flow, these are terms describing bubble coalescence and break-up, as well as the change of the bubble size due to the compressibility of the gaseous phase and phase transition. While the conservation equations are readily derived, source and sink terms have to be modeled, either purely in an empirical way or by adopting mechanistic approach.

This requires experiments with a sufficient instrumentation for measuring the interfacial area density, preferably as a field parameter and in transient flows.

Ishii [5] demonstrated that the local time averaged interfacial area density (IAD) is equal to the sum of the inverse of individual velocities of all phase boundaries passing through a point in space, corrected by the cosine of the individual attack angle of the interface and divided by the measuring time:

$$\overline{a_{x,y,z}} = \frac{1}{t_m} \sum_{i=1}^{n_i} \frac{1}{v_i \cdot cos(\varphi)} \tag{1}$$

This discovery opened the pathway to the measurement of the interfacial area density by local probes [1]. The minimal configuration to measure velocity and attack angle of an interface is a four-tip probe. Microprobes for such measurements were developed by [6]. Numerous papers deal with the measurement of interfacial area concentrations in vertical pipes, in annular as well as in rectangular channels with both upwards and downwards gas–liquid flow.

Wire-mesh sensors [7] have, compared to local probes, the advantage that they acquire rich information from a two-dimensional domain at once, which can cover an entire flow cross-section. This makes experiments very efficient and allows a direct observation of the topology of the gas-liquid interface by the imaging of the flow patterns. On the other hand, the sensors are known to be more intrusive. Besides void fraction distributions, wire-mesh sensors are used for bubble size measurements, as introduced by [8]. There are also numerous attempts to use them for velocity measurements and to characterize the achievable accuracy [9-14]. In [15] it was demonstrated that wire-mesh sensor data can be processed to provide the interfacial area, as well. There, the gas-liquid interface was reconstructed from the sensor data in a slice-wise way from a time series of individual two-dimensional gas fraction distributions acquired by the sensor. This method was successfully compared to results obtained by four tip probes in a vertical air-water flow [16]. In the present paper, we introduce an alternative method relying on the evaluation of the local void fraction gradient. This is strongly simplifying the data processing compared to methods that reconstruct sharp interfaces from the wire-mesh sensor data, which is by nature limited in its resolution.

2 INTERFACIAL AREA MEASUREMENT USING 3D VOID FRACTION GRADIENTS

2.1 Link between three-dimensional void fraction gradient and interfacial area density

A two-phase flow is completely characterized by a unique time dependent vector field of the fluid velocity, together with the scalar field of the phase indicator function:

$$\vec{w}(x,y,z,t); \quad \phi(x,y,z,t) \tag{2}$$

Both functions are defined on a continuous domain, whereas the phase indicator function has two discrete values, e.g.:

$$\phi(x,y,z,t) = \begin{cases} 0 & \text{if point } (x,y,z) \text{ is occupied by liquid phase in instant } t \\ 1 & \text{if point } (x,y,z) \text{ is occupied by gaseous phase in instant } t \end{cases} \tag{3}$$

The local instantaneous interfacial area density is equal to the absolute value defined as Euclidian norm of the gradient of the phase indicator function:

$$a(x,y,z,t) = \left|\nabla\phi(x,y,z,t)\right| = \sqrt{\left(\frac{\partial\phi}{\partial x}\right)^2 + \left(\frac{\partial\phi}{\partial y}\right)^2 + \left(\frac{\partial\phi}{\partial z}\right)^2} \tag{4}$$

Since the phase indicator is dimensionless, the interfacial area density according to eq. (7) has the right dimension of 1/m, which corresponds to the definition of "interfacial area (in m^2) per unit volume (in m^3)". The concept represented by eq. (4) is of mere theoretical value, since the derivatives of the discrete phase indicator function is either 0 in the bulks of both phases, or infinity at the interface. The phase indicator function is equal to a Heaviside function defined on a linear axis stretching in the direction of the normal vector of the interface; thus the interfacial area density is equal to its derivative and is therefore equal to a Dirac function centered at the location of the interface. An integral over a finite volume of two-phase fluid results in the interfacial area contained in this volume:

$$A = \int_V a(x,y,z,t)dV = \int_V \left|\nabla\phi(x,y,z,t)\right|dV \tag{5}$$

The average interfacial area density in the volume is found by relating the total area A by the volume V, which is basically an arithmetical averaging of the norm of the gradient of the phase indicator function over a control volume:

$$\langle a \rangle = \frac{1}{V}\int_V \left|\nabla\phi(x,y,z,t)\right|dV = \left\langle \left|\nabla\phi(x,y,z,t)\right| \right\rangle \tag{6}$$

The purpose of the wire-mesh sensor is it to deliver local instantaneous volumetric gas fractions from domains defined by the geometry of the sensing element, which is formed by a pair of crossing electrode wires. The ideal reading of the wire-mesh sensor would be an average of the phase indicator function over a sensitive volume formed by the symmetry boundaries of the grids of electrode wires and the sampling time. Supposing a sensor the mid-plane of which is located at z_{WMS}, which is the axial coordinate in a flow duct. Over the cross-section of the duct, transmitter wires are spanned along the y direction and receiver wires along the x direction. The ideal reading of such a sensor can be written as:

$$\varepsilon_{i,j,k,z_{WMS}}^{ideal} = \frac{1}{\Delta x \Delta y \Delta z \Delta t}\int_{x_i-\Delta x/2}^{x_i+\Delta x/2}\int_{y_i-\Delta x/2}^{y_i+\Delta x/2}\int_{z_{WMS}-\Delta z/2}^{z_{WMS}+\Delta z/2}\int_{t_k}^{t_k+\Delta t}\phi(x,y,z,t)dxdydzdt \tag{7}$$

where i and j are the numbers of the transmitter and receiver wires that form the sensitive volume, k is the number of the sample in the time series of measurements, Δx is the pitch of the transmitter wires in the grid, Δy the corresponding pitch of the receiver wires, Δt is the time interval of sampling. In reality, the wire-mesh sensor delivers a signal that is proportional to the conductance present at the crossing point, which is in a general case a complex result of the electrical potential field established between both wires in the presence of liquid and gas separated by a gas-liquid interface. The signal recorded in the presence of a two-phase mixture, related to the signal captured during a calibration with plain liquid and a plain gaseous phase is interpreted as an approximation of the idealized measuring result according to eq. (6):

$$\varepsilon_{i,j,k,z_{WMS}}^{ideal} \approx \varepsilon_{i,j,k,z_{WMS}} = \frac{I_{i,j,liquid} - I_{i,j,k}}{I_{i,j,liquid} - I_{i,j,gas}} \tag{8}$$

Here, $I_{i,j,k}$ is the digital output of the signal acquisition unit of a wire-mesh sensor reflecting the current measured at a crossing point *i,j* at the instant *k* which is reflecting to the conductance of the fluid in the corresponding control volume. It is clear that there is always an uncertainty arising from the hypothesis that the relative conductance reflects the ideal volumetric gas fraction. The main sources of uncertainty are

- the strong non-uniformity of the sensibility within the space between crossing electrode wires resulting in weight of portions of conducting fluid that is increasing the closer they are to the crossing point of wires, which is not reflected by eq. (7),
- the distortion of the potential field between the electrode wires due to the presence of a complex boundary between conducting liquid and practically non-conducting gas,

- the mechanical distortion of the gas-liquid interface due to the interaction with the wires, thus by the intrusivity of the sensor.

A number of papers has dealt with the uncertainty of the wire-mesh sensor. It has been shown that the interpretation of the relative conductance according to eq. (8) as a local instantaneous gas fraction in the sensitive volume formed by a crossing point of wires has an acceptable accuracy for many applications. E.g. volume equivalent bubble diameters can be obtained by integrating the void fraction over a region occupied by the bubble with an uncertainty standing back from the measured value by about an order of magnitude [8]. A comparison with a fast X-ray tomography system also confirmed that void fractions can be measured with an acceptable accuracy [17]. It is obvious that the void fraction according to eq. (7) converges towards the local instantaneous phase indicator function when Δx, Δy, Δz and $\Delta\tau$ tend to zero. Therefore the norm of the gradient of the void fraction converges towards the module of the gradient of the phase indicator function, as well, and thus delivers the local instantaneous interfacial area density:

$$\begin{aligned}\lim_{\substack{\Delta x\to 0\\ \Delta y\to 0\\ \Delta z\to 0\\ \Delta t\to 0}}\left|\nabla\varepsilon_{i,j,k}^{ideal}\right| &= \lim_{\substack{\Delta x\to 0\\ \Delta y\to 0\\ \Delta z\to 0\\ \Delta t\to 0}}\left|\nabla\left[\frac{1}{\Delta x\Delta y\Delta z\Delta t}\int_{x_i-\Delta x/2}^{x_i+\Delta x/2}\int_{y_i-\Delta x/2}^{y_i+\Delta x/2}\int_{z_{WMS}-\Delta z/2}^{z_{WMS}+\Delta z/2}\int_{t_k}^{t_k+\Delta t}\phi(x,y,z,t)\,dx\,dy\,dz\,dt\right]\right| \\ &= \left|\nabla\phi\left(x_i,y_j,z_{WMS},t_k\right)\right| = a\left(x_i,y_j,z_{WMS},t_k\right)\end{aligned} \tag{9}$$

It can therefore be postulated that the norm of the gradient of the void fraction measured by the wire-mesh sensor provides an approximation of the interfacial area density averaged over the sensitive volume formed by a given crossing-point:

$$\left|\nabla\varepsilon_{i,j,k,z_{WMS}}\right| \approx \frac{1}{\Delta x\Delta y\Delta z\Delta t}\int_{x_i-\Delta x/2}^{x_i+\Delta x/2}\int_{y_i-\Delta x/2}^{y_i+\Delta x/2}\int_{z_{WMS}-\Delta z/2}^{z_{WMS}+\Delta z/2}\int_{t_k}^{t_k+\Delta t}a(x,y,z,t)\,dx\,dy\,dz\,dt = \overline{a}_{i,j,k,z_{WMS}} \tag{10}$$

There are two issues of additional uncertainties arising from the limited resolution, i.e. from the grid dimensions and the sampling rate of the sensor: (a) the averaging over the control volume in eq. (10) bears an inaccuracy due to the inhomogeneity of the averaged function and a non-uniform distribution of weights, and (b) the void fraction gradient in eq. (10) can only be approximated by finite differences:

$$\overline{a}_{i,j,k,z_{WMS}} \approx \sqrt{\left(\frac{\Delta_x\varepsilon_{i,j,k,z_{WMS}}}{\Delta x}\right)^2+\left(\frac{\Delta_y\varepsilon_{i,j,k,z_{WMS}}}{\Delta y}\right)^2+\left(\frac{\Delta_z\varepsilon_{i,j,k,z_{WMS}}}{\Delta z}\right)^2} \tag{11}$$

Note, that resorting to finite differences causes another contribution to then discretization error, which depends on the applied stencil. In eq. (10) different stencils can be used to calculate the quotients of finite differences. In the analyses discussed below, three different stencils were compared:

Stencil 1:
$$\frac{\Delta_x\varepsilon_i}{\Delta x} = \frac{\varepsilon_{i+1}-\varepsilon_i}{\Delta x} \tag{12}$$

Stencil 2:
$$\frac{\Delta_x\varepsilon_i}{\Delta x} = \frac{\varepsilon_{i+1}-\varepsilon_{i-1}}{2\Delta x} \tag{13}$$

Stencil 3:
$$\frac{\Delta_x\varepsilon_i}{\Delta x} = \frac{-\varepsilon_{i+1}+8\varepsilon_{i+1}-8\varepsilon_{i-1}+\varepsilon_{i-2}}{12\Delta x} \tag{14}$$

In equations (12) to (14), the stencils are described for one coordinate direction. In the other directions y and z, the given rule has to be applied analogically. Stencil 1 is an asymmetric forward stencil of 1st order, while stencil 2 is a symmetric 1st order stencil. The stencil shown in eq. (14) is a symmetric stencil of 2nd

order. The choice of the stencil is not of fundamental importance, but it affects the accuracy of the gradient calculation. For this reason, all three stencils were tested.

2.2 Proof of principle using synthetic discretized void-fraction data

2.2.1 Synthetic bubbles

In order to demonstrate the applicability of the gradient method, the response of a virtual measuring device to a fluid containing a single bubble of well-defined size and shape was used as an input. It was assumed, that the virtual measurement delivers a three-dimensional void fraction array with an equal step-width in all three coordinate directions. Since it is obvious that the result scales with the step width of the measurement in case of geometrical similarity of the assumed bubble, the step width was set to unity, i.e. $\Delta x = \Delta y = \Delta z = \Delta_{WMS} = 1$. A domain with the size of 64 x 64 x 64 voxels was chosen. To start with, in this domain, a spherical bubble of a given diameter was placed and local void fractions were calculated assuming an ideal sensor according to eq. (7). Since a steady-state was analyzed, eq. (7) simplifies to

$$\varepsilon_{i,j,k}^{virtual} = \frac{1}{\Delta x \Delta y \Delta z} \int_{x_i-\Delta x/2}^{x_i+\Delta x/2} \int_{y_i-\Delta x/2}^{y_i+\Delta x/2} \int_{z_k-\Delta z/2}^{z_k+\Delta z/2} \phi(x,y,z)\,dx\,dy\,dk \tag{15}$$

Eq. (15) was calculated numerically. In the essence, $\varepsilon_{i,j,k}^{virtual}$ is the share of the volume of each control volume i,j,k occupied by the gaseous phase, characterized by $\phi(x,y,z)=1$. The boundaries of the bubble are smeared in this process, simulating the limited resolution of a real sensor, as shown in Figure 1.

Figure 1. Synthetic bubbles generated on a 3D grid for the proof of principle

2.2.2 Calculation of the surface area of synthetic bubbles

For simulated bubbles with diameters ranging from $d_{bub} = D_{bub}/\Delta_{WMS} = 0.5$ to 40, the interfacial area was calculated according to eq. (11). The surface area of the virtual bubble is equal to $A_{bub} = \pi D_{bub}^2$. This is compared to the total interfacial area found by summing the areas residing in each voxel:

$$A_{bub,meas} = \sum_{i,j,k} \sqrt{\left(\frac{\Delta_x \varepsilon_{i,j,k}}{\Delta x}\right)^2 + \left(\frac{\Delta_y \varepsilon_{i,j,k}}{\Delta y}\right)^2 + \left(\frac{\Delta_z \varepsilon_{i,j,k}}{\Delta z}\right)^2}\, \Delta x \Delta y \Delta z \tag{16}$$

The result is related to the known surface area by calculating a deviation $\delta = \left(A_{bub,meas} - A_{bub}\right)/A_{bub}$. The result is shown in Figure 2. The symmetrical stencil of 1st order (stencil 2) displays the best result for larger bubbles. In general, the surface of small bubbles is strongly underestimated. The error falls between bands of ±10 % at a relative bubble diameter of $d_{bub} = 3$. With the asymmetric stencil 1, the result converges to an overestimation by 10 % for large spherical bubbles, but the ±10 % band is already

reached at a dimensionless bubble diameter of d_{bub} = 2. The stencil 3 higher order does not result in an improvement.

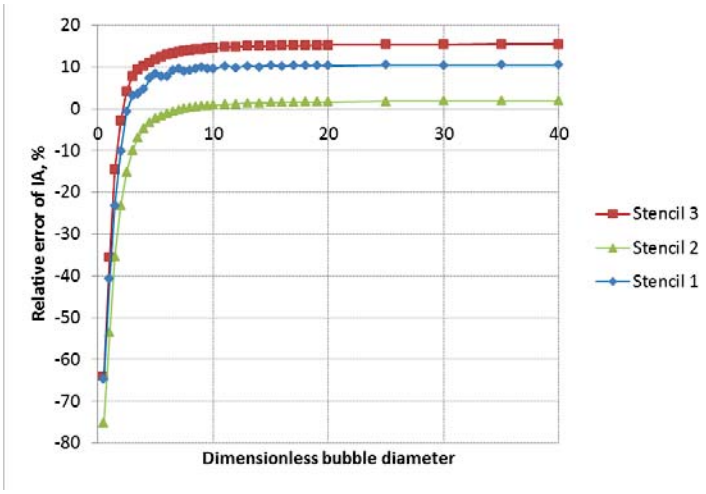

Figure 2. Relative deviation between the interfacial area of a virtual spherical bubble and its value obtained from the module of the void fraction gradient as function of the dimensionless bubble diameter (average of 100 bubbles with random position of the center relative to the grid)

2.2.3 Void fraction signal noise

Signal noise has to have a detrimental effect on the measuring result. Unlike its influence to the bubble size, where it mainly leads to an increase of the statistic uncertainty, it causes a positive bias the interfacial area density. This is because the operation to calculate the norm of the gradient has only positive results, although the sign of the noise effect on each individual vector component of the void fraction gradient is both positive and negative. Noise is caused by electrical disturbance and vibrations of the wires. The relative signal to noise ratio varies for different conductivities of the fluid. It is typically in the range of some percent of the signal amplitude. We studied the effect by adding between 1 and 20 % of Gaussian noise to the void fractions of the synthetic bubbles in a Monte Carlo type calculation and obtained a significant growth in the measured bubble surface (Figure 3).

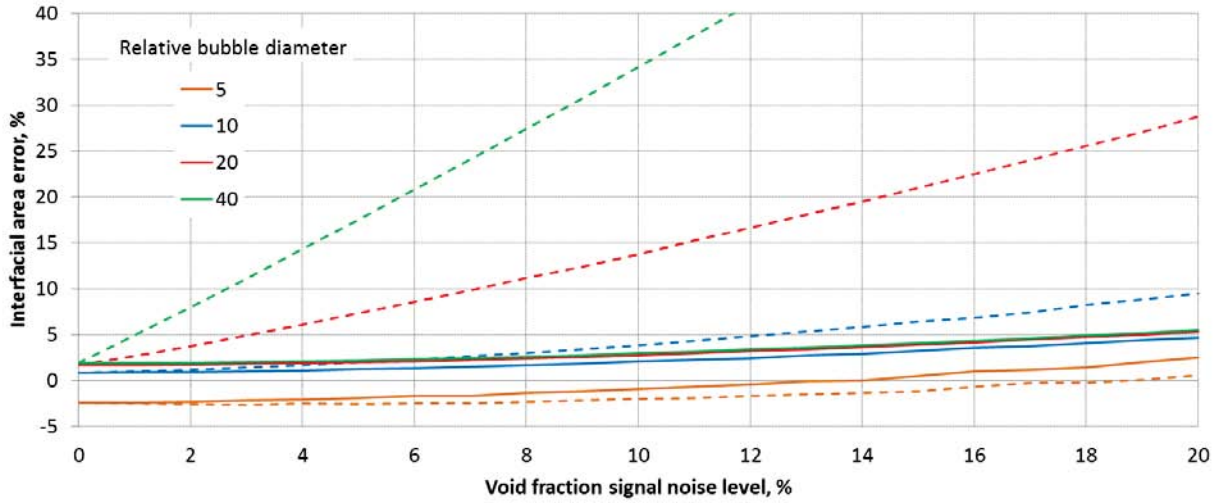

Figure 3. Systematic error of the interfacial area caused by stochastic Gaussian noise superposed to the void fraction signals (dashed lines: noise removed from regions of plain water, solid lines: noise removed additionally from the inside of bubbles, calculations performed using stencil 2)

The dashed lines in Figure 3 represent calculations in which it was assumed that noise is filtered out from all voxels which contain plain water. This is usually possible by a filtering of the raw wire-mesh sensor signals. This is necessary because otherwise usually large domains filled with plain liquid cause a very strong overestimation of the interfacial area. The resulting bias to the interfacial area is depending on the bubble size, because larger bubbles have a smaller surface-to-volume ratio and the noise inside the bubble gets a growing weight. Still, in the range of noise levels below 20 %, which is a kind of a conservative bounding value for practical applications of the wire-mesh sensor, the bias stays below 10 % for relative bubble diameters below $d_{bub} = 10$.

Solid lines are calculated under the assumption that also all voxels containing the plain gaseous phase inside the bubble are without noise, i.e. they are exactly set to a void fraction of 100 %. This is possible after the application of a bubble recognition procedure according to [8]. If the noise is removed also from those points which are identified to lie inside the bubble, the noise bias is significantly reduced. In practice, the noise effect can be sufficiently suppressed.

2.2.4 Elliptical bubbles

This section deals with the influence of the deformation of bubbles. As a first step, synthetic bubbles with the shape of a rotational ellipsoid were analyzed. Bubbles obtain first the shape of an oblate ellipsoid when the departure from a spherical shape starts with growing bubble size. An example of such a bubble is shown in Figure 1 on the right side. In the horizontal plane, the cross-section of the bubble is a circle, i.e. both horizontal semi-principal axes are equal. The ellipticity is defined as the ratio of the vertical semi-principal axis over one of the horizontal axes: $E_{bub} = R_x / R_z = R_y / R_z = D_{bub,V} / D_{bub,H}$. In Figure 4, the ellipticity was varied from 0.05 to 1.95, i.e. covering both oblate and prolate ellipsoids, the latter being of pure theoretical interest.

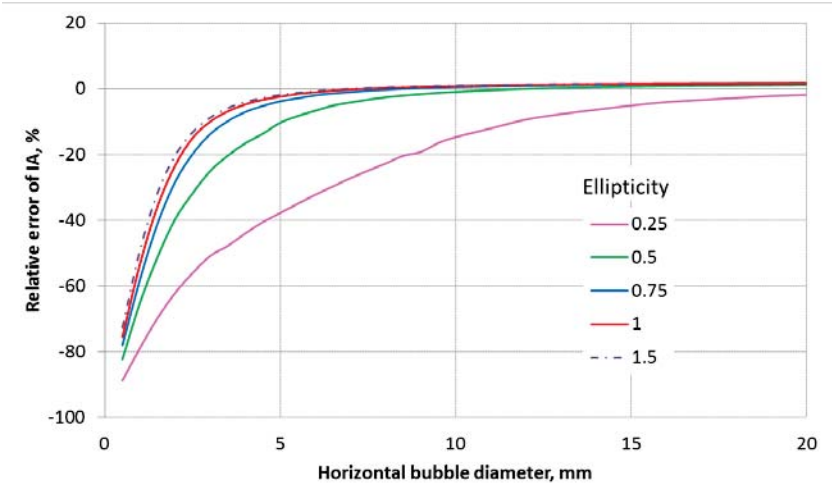

Figure 4. Relative error of the surface area as function of the dimensionless horizontal diameter of a bubble with the shape of a rotational ellipsoid calculated for different ellipticity factors E_{bub} (calculated applying stencil 2)

When the horizontal diameter of an ellipsoidal bubble is kept constant, the underestimation of the interfacial area is larger for higher degrees of flatness. At an ellipticity factor of 0.5, the -10 % band is reached at a dimensionless horizontal diameter of about 5, while the same -10 % band is reached already at a dimensionless diameter of 3 for spherical bubbles. The convergence to the behavior of spherical bubbles is already nearly complete at an ellipticity factor of 0.75 and for prolate bubbles, there is no significant difference to spherical bubbles. In general, one has to be aware of additional uncertainties in case of deformed bubbles.

2.3 Application of the three-layer wire-mesh sensor

A major problem is evident in the term representing the gradient in flow direction. In case of a single wire-mesh sensor with two electrode grids, void fractions are measured only in one plane and a second value from another plane having a certain distance from the first one in the flow direction $\varepsilon_{i,j,k,z_{WMS}+\Delta z}$ is not available. The preferred way to solve this is the application of a three-layer sensor, in which a central grid is used as a grid of transmitter wires, combined with two receiver grids put upstream and downstream of it at a typical axial distance. Such sensor delivers a pair of two-dimensional void fraction distributions $\varepsilon_{i,j,k,z_{WMS}}$ and $\varepsilon_{i,j,k,z_{WMS}+\Delta z}$ simultaneously, which are needed to calculate the z-component of the gradient in eq. (11). In this case, only an asymmetrical stencil of first order can be applied:

$$\frac{\Delta_z \varepsilon_{i,j,k,z_{WMS}}}{\Delta z} = \frac{\varepsilon_{i,j,k,z_{WMS}+\Delta z} - \varepsilon_{i,j,k,z_{WMS}}}{\Delta z} \tag{17}$$

It is known that each wire grid causes a deterioration of the shape of the interface. Therefore, the lateral components are preferentially taken from the first measuring plane. For them, each of the types of stencils (eq. (12) –eq. (14)) can be used. Results for each of the stencils are presented in the following section.

2.4 Experimental validation

2.4.1 Test setup and experimental procedure

For the first experimental test, a three-layer wire-mesh sensor of 3 x 64 wires with a diameter of 100 µm was used. The lateral distance between the wires was $\Delta_{WMS} = \Delta x = \Delta y = 3$ mm in each direction. The axial distance between the grids in flow direction was 3 mm, as well, which means that a $\Delta z = 3$ mm was accepted as the average distance between the pair of measuring planes that the sensor formed. The sensor was put horizontally in a transparent rectangular basin filled with tap water. The water was filled up to a height of 500mm. The wire-mesh sensor was placed at an axial distance of 340 mm from a tube used as air inlet. It had a diameter of 23 mm and was placed 55 mm above the bottom plate. The tube has a downwards facing 90 deg elbow at its end, from which the bubbles were released. This was found to be a reliable way to achieve a periodical production of solitary bubbles which were big enough to fall in the region where the chances are good to obtain the bubble surface from the integration of the module of the void fraction gradient. According to Figure 2, this is the case for bubble diameters larger than at least $d_{bub} = D_{bub}/\Delta_{WMS} > 2$, thus for bubble diameters larger than 6 mm. The generated bubbles had a shape close to wobbling oblate rotational ellipsoids of a lateral extension of about 20 mm and a height of roughly 8-10 mm (Figure 5).

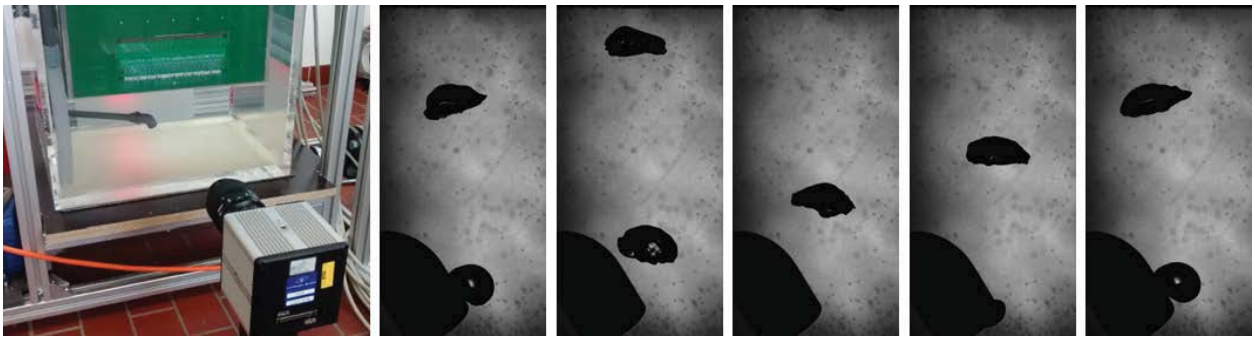

Figure 5. Test basin with high-speed camera and air injection tube (left), sequence of camera images (time step between images 50 ms) of a full bubbling cycle at 0.49 l/min air flow rate

The air volume flow was varied from 0.21 l/min to 0.49 l/min in steps of 0.07 l/min. Data sequences over a measuring time of 10 seconds where recorded at a sampling frequency of 2.5 kHz. The high-speed camera was operated synchronously at a frame rate of 1 kHz. The wire-mesh sensor was located above the aspect region of the camera. A series of selected visualized bubble signals are shown in Figure 6. It was not possible to film the penetration of the bubbles through the sensor directly and a one-by-one comparison of individual bubble detections was not possible. The only way to compare wire-mesh and camera results was a statistic evaluation. It is assumed that the statistic properties of the bubbles stay constant, when experiments are performed at identical air flow rates.

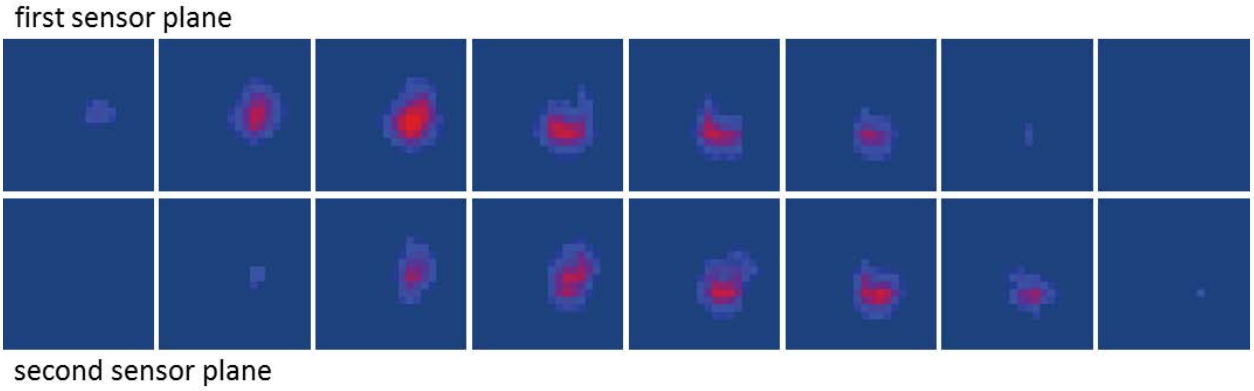

Figure 6. Wire-mesh sensor signals recorded during the passage of a bubble at 0.49 l/min gas injection, time step between images: 8 ms (each 20th sample shown).

2.4.2 Evaluation of high-speed camera sequences

After subtraction of a background image without bubbles, the camera images were binarized and an oblate rotational ellipsoid was adapted to the contour. Both bubble volume and bubble surface area was calculated from the lengths of the semi-major and semi-minor axes. The analysis was repeated for the full image sequence on which a given bubble was present, and the results were averaged. As it can be seen from Figure 7, the scattering of the data is quite high due to the wobbling of the bubbles and due to the fact that only one projection of the bubble shape was evaluated. There is much room for future improvements.

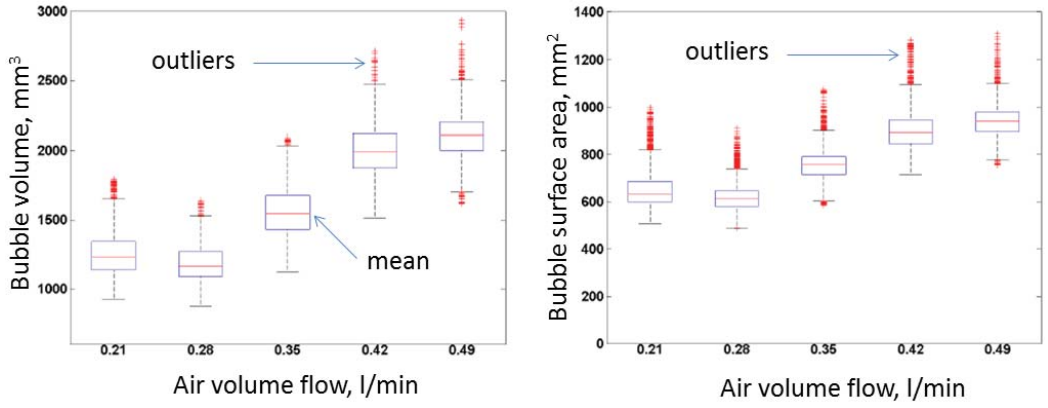

Figure 7. Statistical evaluation of fitted oblate rotational ellipsoids to the bubble images

2.4.3 *Wire-mesh sensor data*

The wire-mesh sensor signals were normalized to the signal levels obtained for plain liquid and plain gas in the sensor according to eq. (8). A sliding average filter of a length of 3 samples was applied to reduce signal noise. We checked the influence of stronger sliding average filters of a length up to 11 time samples and have not found a significant effect on the measuring results. Therefore it was concluded that the applied averaging over 3 samples does not deteriorate the results. Furthermore, signal noise was removed from the plain water regions between the bubbles. The signals were then undergoing a bubble recognition treatment with the extended decremental fill algorithm described in [18]. Bubble velocities w_{bub} were extracted from the time difference between the instants of the appearance of a bubble in the first and the second measuring plane of the sensor (see Figure 6). The velocity information was needed to calculate bubble volumes and to convert interfacial area densities into bubble surface areas.

Local instantaneous interfacial area densities were calculated according to eq. (11) using the axial stencil presented in eq. (17) for the axial direction. The interfacial area density for a bubble was defined as the average over all local interfacial area densities found in the voxels occupied by the bubble. These values cannot be compared directly to the bubble surface area measured by the high-speed camera. For the latter, the area density has to be converted into a surface area by multiplying with the sum of the volumes of all voxels that were identified to be occupied by the given bubble. The volume of a voxel is not equal to the control volume of the gradient determination $\Delta x\Delta y\Delta z$, but is given by the area $\Delta x\Delta y$ multiplied with the distance of propagation of the bubble during one measuring time step, which is w_{bub}/f_{meas}. The surface area of a bubble is therefore found as follows:

$$A_{bub,meas} = \sum_{i,j,k} a_{bub,i,j,k} \Delta x \Delta y \frac{w_{bub}}{f_{meas}} \tag{18}$$

During the measuring period of 10 s, depending on the air flow rate, between 28 and 53 bubbles were recorded. Velocity, volume and surface area of the bubbles were averaged over these ensembles. The results were compared to the average values found with the help of the high-speed camera. In order to get a third independent bubble volume information, the gas flow rate was divided by the average bubble departure frequency calculated by dividing the number of recorded bubbles by the measuring period.

2.4.4 *Experimental results*

Figure 8 shows the comparison of bubble volumes for the different gas flow rates. Wire-mesh results are very close to the volumes obtained from the gas flow rate, while the high-speed camera overestimates bubble volumes significantly. It is in the nature of the error propagation in the formula of the volume of a sphere that the relative deviation for volume equivalent bubble diameters is smaller by a factor of 3.

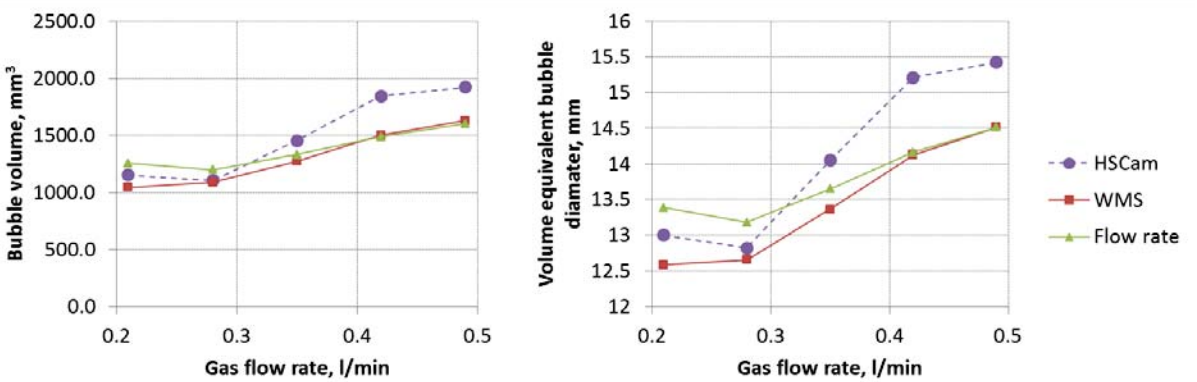

Figure 8. Measured average bubble volume and the corresponding volume equivalent bubble diameter as function of the gas flow rate

The surface area averaged over the available ensembles of bubbles recorded during 10 s of measuring time is be about 20 % lower than the surface area determined from high-speed camera images (Figure 9). We consider this still a very promising result. Please, note that a part of the uncertainty originates from the measuring error of the bubble velocity, which is needed to convert average interfacial area densities into bubble surface areas for the comparison (see eq. (18)). Errors might be reduced by less intrusive sensors with smaller wire diameters and a higher resolution by reducing the electrode pitch D_{WMS}. Another option could be the introduction of correction factors. More work in this direction is needed in the future.

The choice of the stencil for the approximation of the derivatives has not a large influence, which is not completely in line with the findings of the synthetic bubble analyses. Partially, this may be explained by the fact that the stencil can be changed only for the x and y components, but not in z direction. Furthermore, the slopes of the void fraction at the gas-liquid interface are less steep in the real data compared to the synthetic bubbles, which might be another factor reducing the sensibility to the change of the stencil.

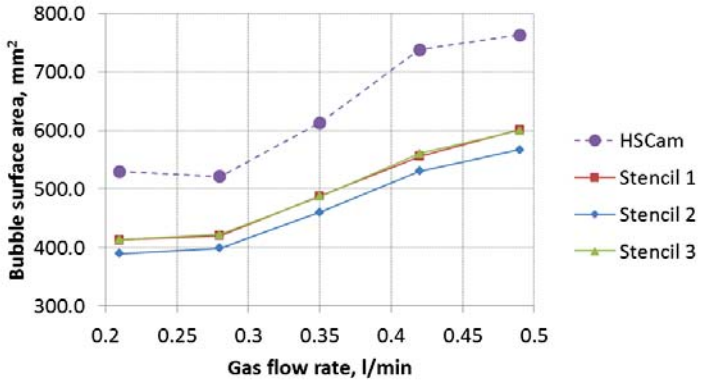

Figure 9. Average bubble surface (interfacial area of a single bubble) obtained by the 3D gradient method compared to the high-speed camera results, as function of the air flow rate

3 APPROXIMAIONS FOR WIRE-MESH SENSORS WITH ONE MEASURING PLANE

3.1 Substitution of the axial gradient component by the time derivative and the bubble velocity

In case that only a single (i.e. two-layer) wire-mesh sensor is available, the substitution of the derivative in z direction by the time derivative and the axial velocity of the moving interface is an alternative:

$$\overline{a}_{i,j,k,z_{WMS}} \approx \sqrt{\left(\frac{\Delta\varepsilon_{i,j,k,z_{WMS}}}{\Delta x}\right)^2 + \left(\frac{\Delta\varepsilon_{i,j,k,z_{WMS}}}{\Delta y}\right)^2 + \left(\frac{\varepsilon_{i,j,k+1,z_{WMS}} - \varepsilon_{i,j,k,z_{WMS}}}{\Delta t} \cdot \frac{\Delta t_m}{w_{i,j,k,z_{WMS}}}\right)^2} \qquad (19)$$

This method poses the additional difficulty to provide information on the velocity, at least an approximate one. It introduces significant additional uncertainties. Nonetheless, the treatment of the available wire-mesh signals according to eq. (19) resulted in a very good agreement with the camera data for the stencils type 2 and 3 (Figure 10), while stencil 1 leads to a significant overestimation of the interfacial area.

The results indicate a general feasibility of the proposed method. First of all, not yet characterized errors of the velocity propagate into the measured interfacial area density and further on the bubble surface area. Secondly, the effective spatial resolution in z direction is equal to the velocity times the sampling period. The bubble velocity was found to be in the range between 0.25 and 0.33 m/s. With a sampling frequency of 2’500 Hz, the effective base length for the finite differences in z direction is only between 0.1 and 0.13 mm, which is much less than the distance between both measuring planes in case of the three-layer sensor

described in the section 2. One can expect that signal noise leads to a much higher positive bias due to this, than the one observed for an equal size of the cell in all three directions (Figure 3).

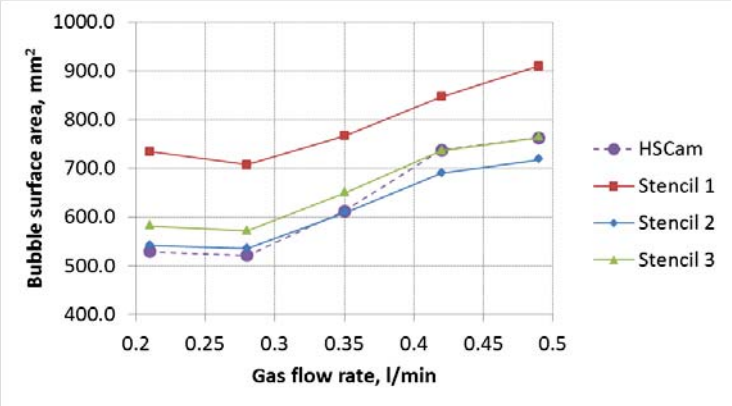

Figure 10. Average bubble surface (interfacial area of a single bubble) obtained by substituting the z component of the spatial gradient by the bubble velocity and the change of void fraction over time (eq. 19)

On the other hand, gradients calculated over a smaller base length Δz are generally more accurate. The ellipticity factor of the bubbles was close to 0.5, judging from the camera images (see Figure 5), whereas the horizontal diameter was in the range of 15 mm. Thus, the dimensionless horizontal diameter at the given lateral pitch between electrode wires of 3 mm was about 5. The theoretical underestimation of bubbles in this range, shown in Figure 5, is about -10 %. The small effective step width arising from the low velocity and the high sampling rate is equivalent to an artificial increase of the ellipticity factor of the bubble, which becomes extremely prolate on the resulting grid. This can be seen as an explanation of about half of the increase of bubble surface observed in Figure 10 compared to Figure 9. More research in needed to give a final answer.

3.2 Estimates of the interfacial area density based on the void fraction gradient in the x-y plane

Another way to navigate around the problem of the missing z component in case of a sensor with only one measuring plane consists in postulating an isotropy of the three components of the gradient vector. Here we rely on the assumption that the contributions of the tree components of the gradient vector to the interfacial area density averaged over a domain of many control volumes are similar. The missing z component would then be substituted by the two available components in x and y direction, multiplied by a correction factor. The surface area of a synthetic bubble according to eq. (16), for example, would be approximated as follows:

$$A_{bub,meas} = C_{corr} \sum_{i,j,k} \sqrt{\left(\frac{\Delta_x \varepsilon_{i,j,k}}{\Delta x}\right)^2 + \left(\frac{\Delta_y \varepsilon_{i,j,k}}{\Delta y}\right)^2}\, \Delta x \Delta y \Delta z \qquad (20)$$

In case of a perfect isotropy of statistically independent gradient vector components one would expect $C_{corr} = \sqrt{3/2}$. The analysis of synthetic bubbles allows determining the correction factor for the simulated bubble shapes using the relation in eq. (21). The result of this operation is shown by the solid lines in Figure 11. It is evident that the correction factor is rather close to the expected value of 1.225 for spherical bubbles, for which ~1.3 is a good approximation. Unfortunately, it is not constant, when the ellipticity is varied. It strongly increases with a decreasing ellipticity factor E. For large bubbles with E = 0.5, a correction factor of 1.8 is a good compromise.

$$C_{corr} = \frac{\sum_{i,j,k} \sqrt{\left(\frac{\Delta_x \varepsilon_{i,j,k}}{\Delta x}\right)^2 + \left(\frac{\Delta_y \varepsilon_{i,j,k}}{\Delta y}\right)^2 + \left(\frac{\Delta_z \varepsilon_{i,j,k}}{\Delta z}\right)}}{\sum_{i,j,k} \sqrt{\left(\frac{\Delta_x \varepsilon_{i,j,k}}{\Delta x}\right)^2 + \left(\frac{\Delta_y \varepsilon_{i,j,k}}{\Delta y}\right)^2}} \tag{21}$$

Note, that the correction needed to arrive at the real value for the bubble surface is of course much higher for small bubbles (dashed lines in Figure 11), since the surface of small bubbles is underestimated even in case of a spherical shape.

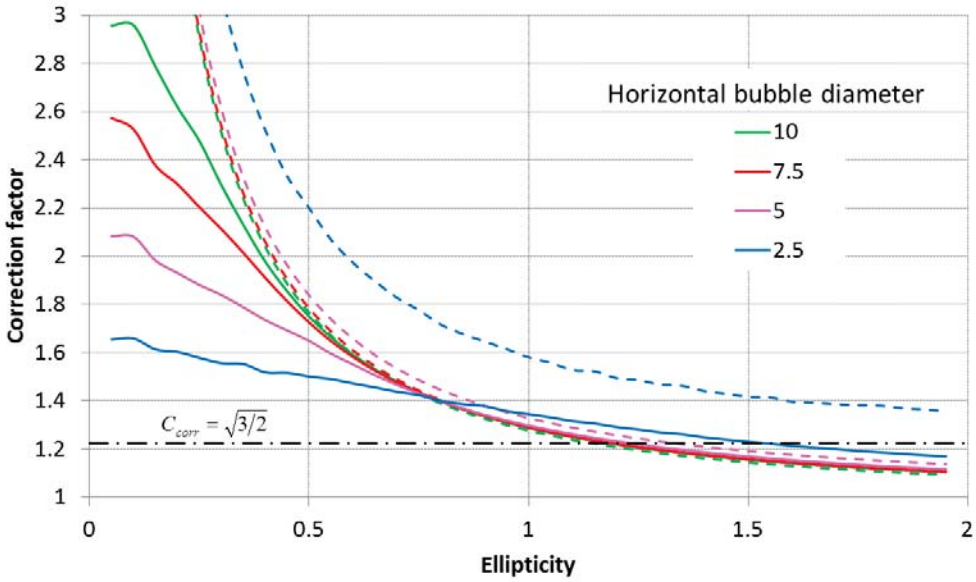

Figure 11. Correction factors for synthetic bubbles of different dimensionless horizontal diameters and different ellipticities (stencil 2 was applied), solid lines – correction factors according to eq. (21), dashed lines – correction factors needed to reproduce the real bubble surface

The experimental data available from the wire-mesh sensor measurements described in the previous section can be used to calculate correction factors by dividing the bubble surface area taken from then high-speed camera images by the integral of the 2D gradient. The result is shown for stencil 2 in Figure 12 on the left side. On the right side, the bubble surface area calculated using the 3D gradient is related to the integral over the 2D gradient. The correction factors were found by a linear regression analysis, under the additional condition that the linear fit passes through the origin of the coordinate system. The value found to match the interfacial areas is about 2 for the first case and about 1.5 for the second. Referring to Figure 11, this would mean that the bubbles correspond to the theoretical cases with ellipticity factors between 0.4 and 0.7, which is a reasonable range.

It can be concluded, that the method of correlate the contribution of the axial component of the void fraction gradient to the interfacial area density to the two lateral components can be envisaged as a way to obtain a first estimate of the interfacial area density if only a two-layer wire-mesh sensor or another measuring method delivering a two-dimensional void distribution is available, e.g. coming from a fast X-ray tomography.

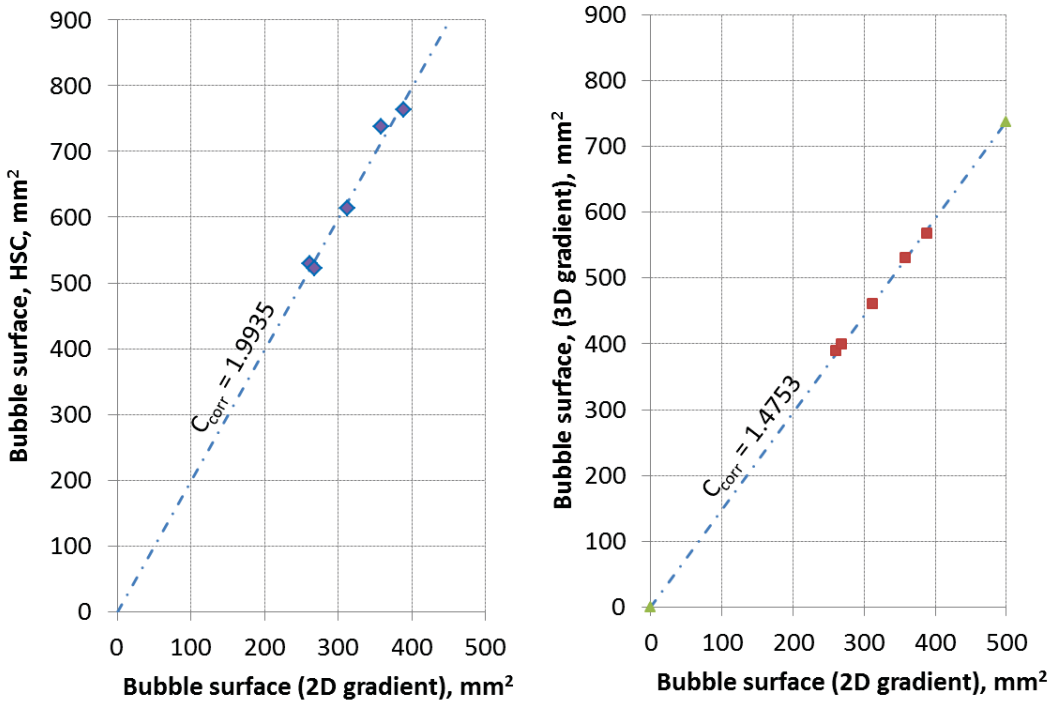

Figure 12. Experimental correction factors for the determination of the interfacial area using x and y components of the void fraction gradient to approximate the z component

4 SUMMARY

Void fraction gradients measured with a wire-mesh sensor can be used to determine the interfacial area concentration in a gas-liquid two-phase flow. If a three-layer sensor is available, all three components of the gradient can be calculated directly. The interfacial area density within a certain domain is then the arithmetical average of the norm of all local void fraction gradients. For the conversion into an interfacial area, the volume of the two-phase flow passing through the measuring plane during the measuring period has to be known, which requires a measurement of the velocity of the interface.

In case of the availability of only one measuring plane, the axial component of the gradient can be substituted by the time derivative and the velocity, or, alternatively, by correlating the effect of the axial component to the other two lateral components. This is accompanied with additional uncertainties, but it can be a way to obtain first estimates, when other methods are not at hand.

The validation was done by comparing bubble diameters and surface areas calculated from wire-mesh sensor data with the same parameters extracted from high-speed camera images. The processing of both the camera data and the wire-mesh sensor signals still deserve further improvements. The paper presents a proof of principle. At the present stage of the studies, a comprehensive uncertainty quantification cannot yet been given. First results obtained by the comparison with the high-speed camera observation allow concluding that the surface area of medium size bubbles ban be reconstructed with an uncertainty one order below the measured quantity. Much more work has to be done by extending the range of bubble sized and improving the quality of the reference measuring method.

An important factor is the velocity measurement. It is planned to compare the bubble velocity measured by the three-layer wire-mesh sensor with the propagation of the bubbles in the camera image sequences.

5 NOMENCLATURE

Variables:

A	Interfacial area, bubble surface	m^2
a	Interfacial area concentration	1/m
D	Diameter	m
d	Relative (dimensionless) Diameter	-
E	Ellipticity factor	-
f	Frequency, sampling rate	Hz, 1/s
R	Radius	m
I	Primary electrical measuring quantity of the sensor (current)	A
t	Time	s
v	Velocity of an interface	m/s
V	Volume	m^3
$\vec{w}$	Velocity vector	m/s
x	Horizontal axis, Cartesian coordinate in the sensor plane	m
y	Horizontal axis, Cartesian coordinate in the sensor plane	m
z	Vertical axis, Cartesian coordinate in flow direction	m
Δ	Electrode pitch	m
δ	Error, deviation	-, %
ε	Volumetric gas fraction, void fraction	-, %
ϕ	Phase indicator function	-
φ	Attack angle of a gas-liquid interface	deg

Indexes, other signs and abbreviations:

bub	Bubbe
H	Horizontal
HSC	High-speed camera
i	Index of the measuring location in the sensor plane in x direction
j	Index of the measuring location in the sensor plane in y direction
k	Index of the current sample in time
meas	Measured quantity
V	Vertical
WMS	Wire-mesh sensor
2D	Two-dimensional
3D	Three-dimensional
Δ	Difference
∇	Nabla operator (here used for obtaining the gradient of a scalar)
$\lvert\ \rvert$	Module, absolute value
$\langle\ \rangle$	Spatial and temporal average

6 REFERENCES

1. Kataoka, I., Ishii, M., Serizawa, A.: Local formulation and measurements of interfacial area concentration in two-phase flow. *Int. J. Multiphase Flow* **12** (1986) 505–529.

2. Hibiki, T., Ishii, M.. Two-group interfacial area transport equations at bubbly-to-slug flow transition. *Nucl. Eng. Des.* **202** (2000) 39–76.
3. Fu, X.Y., Ishii, M.,. Two-group interfacial area transport in vertical air/water flow. I. Mechanistic model. *Nucl. Eng. Des.* **219** (2002) 143–168.
4. Fu, X.Y., Ishii, M.: Two-group interfacial area transport in vertical air/water flow. II. Model evaluation. *Nucl. Eng. Des.* **219** (2002) 169–190.
5. Ishii, M.: Thermo-Fluid Dynamic Theory of Two-Phase Flow. *Eyrolles*, Paris, 1975.
6. Kim, S., Ishii, M.: Micro four-sensor probe measurement of interfacial area transport for bubbly flow in round pipes. *Nucl. Eng. Des.* **205** (2001) 123-131.
7. Prasser, H.-M., Böttger, A., Zschau, J.: A new electrode–mesh tomograph for gas–liquid flows. *Flow Meas. Instrum.* **9** (1998) 111–119.
8. Prasser, H.-M., Scholz, D., Zippe, C.: Bubble size measurement using wire–mesh sensors. *Flow Meas. Instrum.* **12** (2001) 4, 299–312.
9. Richter, S., Aritomi, M., Prasser, H.-M., Hampel, R.: Approach towards spatial phase reconstruction in transient bubbly flow using a wire-mesh sensor, *International Journal of Heat and Mass Transfer* **45** (2002), 1063-1075.
10. W. Wangjiraniran, Y. Motegi, S. Richter, H. Kikura, M. Aritomi, K. Yamamoto: Intrusive Effect of Wire Mesh Tomography on Gas-liquid flow measurement, *Journal of Nuclear Science and Technology*, **40** (2003) 11, 932-940
11. Ito, D., Prasser, H.-M., Kikura, H., Aritomi, M.: Uncertainty and intrusiveness of three-layer wire-mesh sensor, *Flow Measurement and Instrumentation*, **22** (2011) 4, 249-256
12. M. Simiano, H.-M. Prasser, Estimation of individual bubble velocities in a gas-liquid flow using wire-mesh sensors, *6th International Conference on Multiphase Flow, ICMF*, Leipzig, Germany, July 9-13, 2007.
13. T. Kanai, M. Furuya, T. Arai, K. Shirakawa, Y. Nishi: Three-dimensional phasic velocity determination methods with wire-mesh sensor, *International Journal of Multiphase Flow* **46** (2012) 75-86.
14. D. Hoppe, A. Grahn, P. Schütz: Determination of velocity and angular displacement of bubbly flows by means of wire-mesh sensors and correlation analysis, *Flow Measurement and Instrumentation* **21** (2010) 48-53.
15. H.-M. Prasser, M. Beyer, H. Carl, S. Gregor, Dirk. Lucas, H. Pietruske, P. Schütz, F.-P. Weiss: Evolution of the structure of a gas-liquid two-phase flow in a large vertical pipe, *Nuclear Engineering and Design* **237** (2007) 1848-1861.
16. A. Manera, B. Ozar, S. Paranjape, M. Ishii, H.-M. Prasser, Comparison between wire-mesh sensors and conductive needle-probes for measurements of two-phase parameters, *Nuclear Engineering and Design* **239** (2009) 1718-1724.
17. Prasser, H.-M., Misawa, M., Tiseanu, I.: Comparison between wire-mesh sensor and ultra-fast X-ray tomograph for an air-water flow in a vertical pipe, Flow Measurement and Instrumentation 16 (2005), 73–83.
18. Prasser, H.-M.; Beyer, M.: Bubble recognition algorithms for the processing of wire-mesh sensor data, *6th International Conference on Multiphase Flow, ICMF*, July 09-13, 2007 Leipzig, pp. 719.